RSC Advances

PAPER

View Article Online
View Journal | View Issue

Cite this: *RSC Adv.*, 2025, **15**, 29089

An aluminum-based adsorbent/zeolite molecular sieve composite for the sorption of lithium in the salt lake

Dawei Fang, [a] Shilong Suo,[a] Donglu Fu,*[b] Kunhao Liang,[c] Jing Qiao*[ac] and Zongren Song *[a]

In the context of the global energy transition, the efficient extraction of lithium resources has become a critical link in the new energy industry chain. Addressing challenges such as poor selectivity, low adsorption capacity, and environmental concerns in extracting lithium from salt lake brines, this study developed a novel aluminum-based adsorbent/zeolite molecular sieve composite adsorbent (LiAl-LDHs/ZSM-5). The material was constructed with a hierarchical porous structure through seed-assisted synthesis of the ZSM-5 molecular sieve carrier, followed by *in situ* hydrothermal growth of lithium-aluminum layered double hydroxide (LiAl-LDHs). Systematic characterization *via* XRD, FT-IR, and SEM confirmed its crystal structure, functional group distribution, and micro-morphology. Single-factor experiments optimized key parameters (ZSM-5 : LiAl-LDHs = 1 : 2) and adsorption conditions (pH = 7, T = 25 °C, C = 10 g L^{-1}). Kinetic analysis revealed that the adsorption conformed to the pseudo-second-order model, indicating chemisorption-dominated mechanisms. The composite demonstrated high selectivity (αLi Mg = 188.13) and recyclability in authentic salt lake brine, offering an environmentally friendly solution for exploiting high Mg^{2+}/Li^{+} ratio resources.

Received 20th July 2025
Accepted 11th August 2025

DOI: 10.1039/d5ra05236j

rsc.li/rsc-advances

1. Introduction

Lithium compounds are extensively utilized in ceramics, nuclear materials, glass manufacturing, pharmaceuticals, and battery production industries.[1–3] The rapid expansion of electric vehicles and grid-scale energy storage has substantially increased lithium demand for batteries.[4–6] Compared to ore-based extraction (*e.g.*, spodumene), lithium recovery from salt lake brines reduces costs by 30–50% while offering environmental advantages.[7] However, both brine and seawater systems contain coexisting ions (Na^{+}, K^{+}, Ca^{2+}, Mg^{2+}), where efficient Li^{+}/Mg^{2+} separation remains challenging due to their similar crystal ionic radii (Li^{+}: 0.076 nm; Mg^{2+}: 0.072 nm).[8] Globally, major lithium-rich salt lakes are distributed in Chile, Argentina, Bolivia, the United States, and China. While brine resources in the first four countries typically exhibit Mg^{2+}/Li^{+} mass ratios <8.0,[9] Chinese salt lakes—despite harboring >85% of domestic lithium reserves—face inherent challenges of ultrahigh Mg^{2+}/Li^{+} ratios (>40).[10] Current domestic lithium production fails to meet escalating strategic demands, necessitating breakthroughs in cost-effective extraction technologies for high-Mg^{2+}/Li^{+} ratio brines to achieve resource self-sufficiency.

Lithium extraction from primary resources faces high energy consumption bottlenecks. Electrodialysis (ED), as an energy-efficient and eco-friendly technology, utilizes electrical potential gradients to achieve electrolyte desalination and concentration, demonstrating various advantages for lithium salt enrichment.[11] Compared to conventional calcination methods, ED offers superior ion selectivity with lower energy demands, particularly for low-concentration lithium solutions.[12,13] Selective electrodialysis (SED) employing monovalent ion-selective membranes has emerged as a promising technique for high Mg^{2+}/Li^{+} ratio brines, with Nie *et al.*[14] reporting >90% Li^{+} recovery. Nanofiltration (NF), a pressure-driven membrane process, enables selective Mg^{2+}/Li^{+} separation through charged group repulsion. Somrani *et al.*[15] confirmed that NF90 membranes achieve efficient lithium extraction. Nevertheless, ED/NF technologies remain constrained by competitive ion effects, concentration polarization, and energy limitations. While traditional precipitation methods offer low-cost industrialization potential, they are only viable for low Mg^{2+}/Li^{+} ratio brines.[16] Solvent extraction exhibits remarkable selectivity for high Mg^{2+}/Li^{+} systems: tributyl phosphate (TBP)-based extractants enable efficient Mg^{2+}/Li^{+} separation[17–19] but suffer from equipment corrosion, third-phase formation, and solvent residue.[20–22] Crown ether extractors face scalability challenges due to prohibitive cost.[23] Although TBP-MIBK systems achieve

[a]*Institute of Rare and Scattered Elements, College of Chemistry, Liaoning University, Shenyang, Liaoning 110036, China. E-mail: zongrensong@lnu.edu.cn*
[b]*Shenyang Institute of Science and Technology, Shenyang, Liaoning, 110167, China*
[c]*School of Opto-Electronic Engineering, Zaozhuang University, Zaozhuang, Shandong 277160, China*

98% lithium recovery, solvent regeneration incurs additional expenses. Developing cost-efficient lithium recovery technologies thus represents a critical solution to global lithium shortages.[24,25]

In recent years, adsorption has emerged as a pivotal approach for lithium extraction from low-grade brines due to its environmental and economic merits, with high-performance adsorbent development being central to this technology. Manganese-based ion sieves (such as $LiMn_2O_4$) exhibit superior selectivity but suffer from structural instability, where acid treatment triggers manganese dissolution.[26,27] Although doping,[28,29] nano structuring,[30] or electrochemical assistance[31,32] can mitigate these issues, industrial deployment remains constrained. Titanium-based adsorbents (*e.g.*, lithium titanate, LTO) demonstrate exceptional cycling stability, with Lawagon *et al.*[8] reporting Li^+/Mg^{2+} separation factors up to 333.2, while the production cost of LTO is expensive. Fe-doped LTO developed by Wang *et al.*[33] achieves high capacity but suffers from poor permeability in powder form, necessitating porous granulation[34] or nanotube synthesis[35] for engineering applicability. Aluminum salt adsorbents (LiAl-LDHs) enable Li^+-specific capture *via* layered vacancy structures, where the "memory effect" and "steric hindrance effect" confer ultrahigh Mg^{2+}/Li^+ selectivity.[36,37] Magnetic modification further enhances separation performance.[38] However, the practical adsorption capacity of LiAl-LDHs was consistently lower than the theoretical capacity.[39] Therefore, improvement in the Li adsorption capacity of LiAl-LDH has become a challenge to foster further progress of the Li extraction industry. Early resin-supported versions incur high costs, while directly synthesized variants show limited capacity, demanding synergistic enhancement with molecular sieves. ZSM-5 molecular sieves with high Si/Al ratios, large surface areas, and shape-selective catalysis are well-established in catalytic cracking[40] and alkylation.[41] Recent studies extend their utility to environmental adsorption, where Zuo *et al.*[42] demonstrated that high-silica ZSM-5 (HSZSM-5) efficiently removes sulfonamide antibiotics *via* liquid-film diffusion mechanisms, highlighting its potential as an adsorbent carrier. Silva *et al.*[43] successfully loaded biomass materials onto ZSM-5 molecular sieves and applied the resulting composite to Cr(VI) adsorption. Experimental results demonstrated the exceptional ion-exchange capacity of this composite, unequivocally validating the feasibility of such hybrid materials for metal ion adsorption applications. The hydrothermal *in situ* loading of aluminum-based adsorbents onto seed-assisted ZSM-5 carriers offers a notable advancement in lithium extraction from high Mg^{2+}/Li^+ ratio brines. This composite design leverages the structural and chemical synergy between LiAl-LDHs and ZSM-5. The high surface area and abundant silanol groups of ZSM-5 enhance the dispersion and accessibility of active sites. Its rigid framework provides structural support, mitigating layer collapse of LiAl-LDHs through a nano-confinement effect. Moreover, the interconnected pore channels of ZSM-5 facilitate rapid lithium-ion transport while complementing the ion-selective adsorption of LiAl-LDHs, together improving separation efficiency and material permeability. This strategy effectively addresses the stability and diffusion limitations of conventional LiAl-LDHs adsorbents.

Addressing ecological fragility and compositional complexity in lithium extraction from western China's salt lakes, this work pioneers an innovative strategy of integrating aluminum salt adsorbents (LiAl-LDHs) with ZSM-5 molecular sieves. Through *in situ* hydrothermal loading of LiAl-LDHs onto seed-assisted synthesized ZSM-5 carriers, we constructed a novel LiAl-LDHs/ZSM-5 composite adsorbent designed to overcome the traditional capacity limitations of aluminum salts and enhance permeability. Systematic optimization of ZSM-5/LiAl-LDHs mass ratios and adsorption parameters (time, temperature, pH, and solid–liquid ratio) was conducted. Material formation mechanisms were elucidated *via* XRD crystallography, FT-IR functional group analysis, and SEM morphological characterization. The composite demonstrated exceptional cyclic stability and ion selectivity (particularly Li^+/Mg^{2+} separation efficiency) in authentic salt lake brines. Adsorption kinetics modeling further revealed mass transfer mechanisms. This study provides a new paradigm for developing high-capacity, readily regenerable, and environmentally benign adsorbents, enabling sustainable exploitation of high-Mg^{2+}/Li^+ ratio brine resources.

2. Experimental

2.1 Reagents

Manganese carbonate ($MnCO_3$), hydrochloric acid (HCl), and sulfuric acid (H_2SO_4) were purchased from Tianjin Damao Chemical Reagent Factory (China). Aluminium nitrate nonahydrate ($Al(NO_3)_3 \cdot 9H_2O$) and sodium aluminate ($NaAlO_2$) were purchased from Tianjin Fuyu Chemical Reagent Factory (China). Lithium nitrate ($LiNO_3$), urea (CH_4N_2O), ethyl orthosilicate (TEOS, $(C_2H_5O)_4Si$), anhydrous ethanol (EtOH, C_2H_5OH), tetrapropylammonium hydroxide (TPAOH, $C_{12}H_{29}NO$), and silica sol ($SiO_2 \cdot nH_2O$) were purchased from Shanghai Macklin Biochemical Co., Ltd (China). Salt-lake brine samples were collected from Baqiancuo salt-lake (Tibet, China). The composition of the salt-lake brine used in the experiment is shown in Table 1.

2.2. Preparation of the ion sieves

2.2.1 Synthesis of silicalite-1 seed. Nano-silicalite-1 seeds were hydrothermally crystallized (120 °C, 48 h) from a gel (molar ratio $SiO_2 : TPAOH : EtOH : H_2O : Na_2O = 2 : 0.5 : 8 : 20 : 0.05$) prepared by sequential addition of TEOS (41.66 g) and ethanol (36.85 g), NaOH (0.4 g), H_2O (36 g), and dropwise TPAOH (10.16 g) under 24 h stirring. The product was quenched, centrifuged, washed, dried (80 °C, 12 h), and pulverized.

2.2.2 Synthesis of ZSM-5 zeolite. ZSM-5 was synthesized *via* staged hydrothermal crystallization from a gel ($Na_2O : SiO_2 :$

Table 1 Concentration of the element in salt-lake brine

Element	B	Ca	K	Li	Mg	Na
mg L^{-1}	472	335	2749	388	2948	22 706

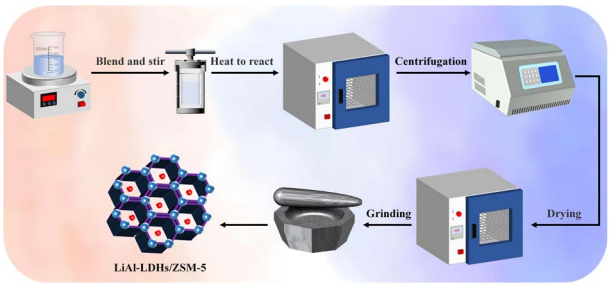

Fig. 1 Preparation process of LiAl-LDHs/ZSM-5.

$Al_2O_3 : H_2O = 10.3 : 100 : 1.25 : 2500$). NaOH (0.76 g) and Al_2O_3 (0.43 g) dissolved in H_2O (42.86 g) were mixed with silica sol (15.94 g, 5 h stirring), then seeded with 0.6 wt% silicalite-1 (1 h stirring). The solid was quenched, centrifuged, washed, dried (80 °C, 12 h), and pulverized.

2.2.3 Synthesis of LiAl-LDHs/ZSM-5 composite. LiAl-LDHs/ZSM-5 was prepared by dissolving $Al(NO_3)_3 \cdot 9H_2O$ and $LiNO_3$ (Al : Li = 2) in H_2O, adding urea (urea : metal ions = 3) and ZSM-5 (zeolite : Li^+ = specified ratio), homogenizing (1 h), and hydrothermally treating (120 °C, 24 h). The composite was washed, dried (80 °C), and pulverized. The synthesis protocol is schematically illustrated in Fig. 1.

2.3 Characterization of ion sieves

Material characterization was performed as follows: X-ray diffraction (XRD) analysis employed Cu Kα radiation (40 kV, 25 mA) with a 2θ range of 5–80° at a 4° min^{-1} scan rate to determine the phase composition of both pristine and modified aluminum salt adsorbents. Fourier-transform infrared (FT-IR) spectroscopy identified functional groups and bonding configurations. Scanning electron microscopy (SEM) revealed morphological features and surface architectures. Lithium ion concentrations before/after adsorption were quantified using atomic absorption spectroscopy (AAS), with measurements conducted in triplicate.

2.4 Adsorption experiments

The LiAl-LDHs/ZSM-5 composite, synthesized with a mass ratio of $Al(NO_3)_3 \cdot 9H_2O$ to $LiNO_3 = 2$ and zeolite-to-Li^+ ratio = 2, was evaluated for lithium adsorption. Before/after adsorption, brine samples were analyzed *via* atomic absorption spectroscopy (AAS) to determine Li^+ concentration. The equilibrium adsorption capacity (Q_e, mg g^{-1}) was calculated as:

$$Q_e = \frac{(C_0 - C_e) \times V}{m} \quad (1)$$

where C_0 is the initial Li^+ concentration (mg L^{-1}), C_e is the equilibrium Li^+ concentration (mg L^{-1}), V is the solution volume (L), and m is the adsorbent dosage (g).

$$K_d = \frac{(C_0 - C_e) \times V}{C_e m} \quad (2)$$

$$\alpha_{Me}^{Li} = \frac{K_d(Li)}{K_d(Me)} \quad (3)$$

$$C_F = \frac{Q_e(Me)}{C_0(Me)} \quad (4)$$

where C_F is the concentration factor (mL g^{-1}); K_d is the distribution factor (mL g^{-1}); α_{Me}^{Li} is the separation coefficient; C_{Me} denotes the concentrations of various ions in the salt-lake brine (mg L^{-1}); Me represents Ca^{2+}, Mg^{2+}, Na^+, K^+, B^{3+} and Li^+ respectively.

2.5 Desorption experiments

A 0.5 g sample of LiAl-LDHs/ZSM-5 composite was dispersed in 10 mL deionized water (pH = 7) and subjected to desorption at 60 °C for 9 h in a constant-temperature water bath with 200 rpm agitation. Desorption efficiency (W, %) was calculated by comparing the adsorbed Li^+ quantity (from adsorption experiments) with desorbed Li^+ content in the eluent, where Li^+ concentration was quantified *via* atomic absorption spectroscopy (AAS) according to:

$$W = \frac{C_s}{C_0 - C_e} \times 100\% \quad (5)$$

where C_s is the Li^+ concentration in the eluent (mg L^{-1}), C_0 and C_e represent initial and equilibrium Li^+ concentrations (mg L^{-1}) from adsorption experiments, V denotes solution volume (L), and m is adsorbent mass (g).

2.6 Adsorption kinetics

Adsorption kinetics employs mathematical models to describe dynamic evolution toward equilibrium under multifactorial influences. Given the inherent complexities—including adsorbent heterogeneity, diverse target ions, variable media composition, and environmental fluctuations (such as ambient and elevated temperatures)—single-theory approaches prove insufficient for comprehensive analysis. In solid–liquid systems, adsorption rates are typically modeled using three primary equations: the pseudo-first-order, pseudo-second-order, and Weber–Morris (W–M) kinetic models.

Pseudo-first-order kinetic model:

$$\ln(Q_e - Q_t) = \ln Q_e - K_1 \times t \quad (6)$$

Pseudo-second-order kinetic model:

$$\frac{t}{Q_t} = \frac{1}{K_2} \times \frac{1}{Q_e^2} + \frac{t}{Q_e} \quad (7)$$

where Q_e (mg g^{-1}) is the Li^+ adsorption capacities at equilibrium; Q_t (mg g^{-1}) is the lithium adsorption capacity at time t; K_1 (min^{-1}) and K_2 (g mg^{-1} min^{-1}) are the adsorption constants.

To further investigate intra-particle diffusion during adsorption, kinetic data were analyzed using the Weber–Morris (W–M) intraparticle diffusion model. The simplified W–M equation is expressed as:

$$Q_t = K_3 \times t^{0.5} + B \quad (8)$$

where B is the parameter representing the boundary layer, and K_3 (mg g^{-1} $min^{-0.5}$) denotes the intraparticle diffusion rate

constant. The constant K_3 is determined from the slope of linear regression in Q_t *versus* $t^{0.5}$.

3. Results and discussion

3.1 Characterization of adsorbent

Comparative SEM analysis of LiAl-LDHs and ZSM-5 elucidates their structural characteristics and synergistic functionality in lithium extraction from salt lakes. Fig. 2a reveals uniformly distributed ZSM-5 particles (1–3 μm) exhibiting smooth surfaces, regular hexagonal morphology, and predominant pupa-like crystalline structures. Fig. 2b demonstrates well-dispersed LiAl-LDHs spheres (200–500 nm) composed of distinctly stacked nanolayers with structural integrity. The composite morphology in Fig. 2c confirms successful LiAl-LDHs loading onto ZSM-5, transforming originally smooth zeolite surfaces into coarse textures with granular deposits. High-magnification imaging (Fig. 2d) resolves these surface features as densely packed layered structures characteristic of LiAl-LDHs, verifying effective heterostructure formation. This nano-architectural integration provides additional active sites, enhancing metal ion capture efficiency from brines compared to individual components. The synergistic adsorption mechanism elevates lithium recovery rates, positioning LiAl-LDHs/ZSM-5 as a promising adsorbent for industrial brine processing.

FT-IR analysis in Fig. 3a confirms successful ZSM-5 synthesis through characteristic vibrations: a strong peak at 1086.73 cm^{-1} (Si–O–Si asymmetric stretching), 735.83 cm^{-1} (Si–O symmetric stretching), 539.35 cm^{-1} (Al–O–Si bending), and 443.44 cm^{-1} (Si–O–Al bending). The broad intense peak at 3421.78 cm^{-1} arises from O–H stretching vibrations, attributed to hydroxyl groups introduced during hydrothermal synthesis, with peak broadening enhanced by intra/intermolecular hydrogen bonding and interlayer water within the lithium–aluminum layered structure.[44] A minor peak at 1373.36 cm^{-1} suggests trace CO_3^{2-} incorporation from atmospheric CO_2 intercalation during synthesis. Additional framework vibrations at 1220.23 cm^{-1}, 1087.24 cm^{-1}, 734.87 cm^{-1}, 543.93 cm^{-1}, and 446.36 cm^{-1} correspond to fundamental T–O–T (T = Si/Al) tetrahedral modes: 1087.24 cm^{-1} (T–O–T asymmetric stretch), 734.87 cm^{-1} (T–O symmetric stretch), and 446.36 cm^{-1} (T–O bending).[45]

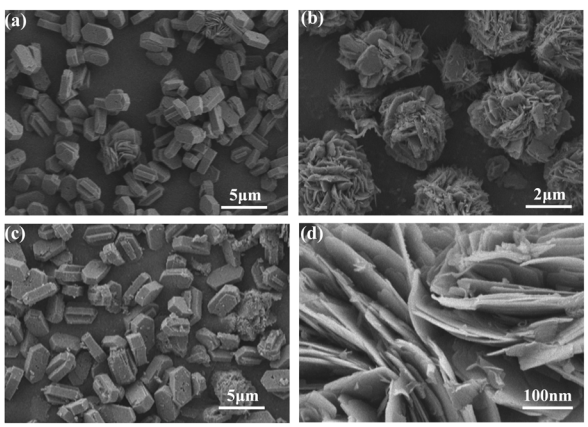

Fig. 2 (a) SEM image of ZSM-5, (b) LiAl-LDHs; and (c) and (d) LiAl-LDHs/ZSM-5.

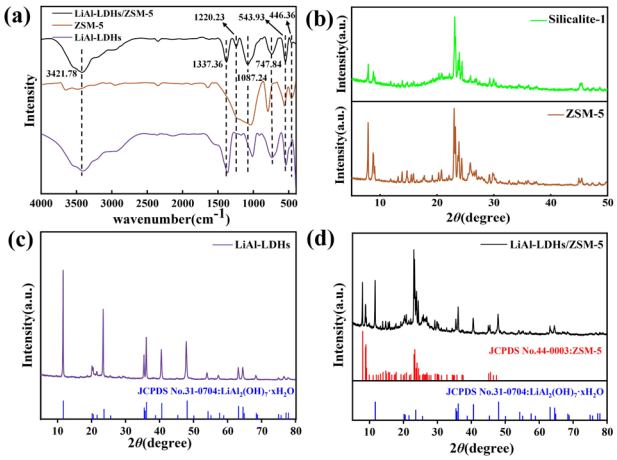

Fig. 3 (a) FTIR patterns of ZSM-5, LiAl-LDHs, LiAl-LDHs/ZSM-5, XRD patterns of (b) silicalite-1, ZSM-5, (c) LiAl-LDHs, and (d) LiAl-LDHs/ZSM-5.

Fig. 3b confirms successful synthesis of nano-silicalite-1 seeds, with distinct XRD reflections at $2\theta = 7.8^\circ$, 8.8°, 23.2°, 23.8°, and 24.3° matching the standard MFI topology. Persistent high-intensity peaks at $2\theta = 7.9 \pm 0.1^\circ$, $8.8 \pm 0.1^\circ$, $23.1 \pm 0.1^\circ$, $23.8 \pm 0.1^\circ$, and $24.3 \pm 0.1^\circ$ further validate the high crystallinity and phase-pure MFI structure of the synthesized ZSM-5 molecular sieve.[45] As evidenced in Fig. 3c, the hydrothermal-derived aluminum salt adsorbent exhibits XRD patterns identical to $LiAl_2(OH)_7 \cdot xH_2O$, confirming its dominant component as lithium–aluminum layered hydroxide.[46] Fig. 3d reveals preserved MFI topology in the composite through characteristic reflections at $2\theta = 7.9 \pm 0.1^\circ$, $8.8 \pm 0.1^\circ$, $23.1 \pm 0.1^\circ$, $23.8 \pm 0.1^\circ$, and $24.3 \pm 0.1^\circ$, while $LiAl_2(OH)_7 \cdot xH_2O$ signatures from LiAl-LDHs remain detectable. Notable intensity attenuation of ZSM-5 peaks, coupled with minimal peak shifts ($<0.2^\circ$), demonstrates effective LiAl-LDHs loading without compromising the zeolitic framework integrity, confirming successful composite formation.

3.2 Composite ratio of materials

The mass ratio of composite components critically governs adsorption performance. As depicted in Fig. 4a, adsorption capacity follows a bell-shaped curve with increasing ZSM-5 content: initial enhancement transitions to decline beyond an optimal threshold. This trend originates from competing mechanisms—moderate ZSM-5 incorporation facilitates effective LiAl-LDHs loading, whereas excess ZSM-5 (>1 : 2 ratio) induces active site dilution and structural heterogeneity. Consequently, the LiAl-LDHs : ZSM-5 mass ratio of 1 : 2 delivers peak performance with a calculated capacity of 4.00 mg g^{-1}.

3.3 Time

Fig. 4b reveals rapid exponential growth in adsorption capacity during the initial 240 min for LiAl-LDHs/ZSM-5, attributable to

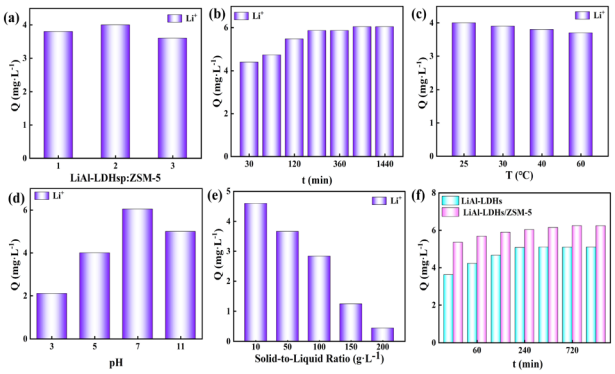

Fig. 4 Effect of (a) composite ratio of materials, (b) time, (c) temperature, (d) pH, (e) solid-to-liquid ratio on adsorption capacity using LiAl-LDHs/ZSM-5; (f) comparison of adsorption performance of LiAl-LDHs/ZSM-5 and LiAl-LDHs.

abundant vacant sites facilitating unrestricted Li^+ intercalation. Subsequent plateau formation beyond 240 min indicates restricted adsorption kinetics due to structural reorganization and pore narrowing caused by accumulated Li^+. Equilibrium was achieved after 12 h, yielding an optimal adsorption capacity of 6.06 mg g^{-1}. This represents a discernible enhancement over coprecipitation-synthesized aluminum salt adsorbents and pristine LiAl-LDHs, demonstrating the composite's structural superiority.

3.4 Temperature

Fig. 4c indicates that temperature exerts a less pronounced influence on LiAl-LDHs/ZSM-5 adsorption compared to other factors. While thermal effects are observable, they are not decisive for adsorption performance. Considering industrial cost-efficiency and energy-saving benefits, the optimal adsorption temperature was selected as 25 °C (ambient conditions), yielding a calculated capacity of 4.00 mg g^{-1}.

3.5 pH

Fig. 4d indicates enhanced adsorption performance of LiAl-LDHs/ZSM-5 in weakly alkaline environments (pH = 3–11), with deviations from pH 7 significantly reducing efficiency due to competing reactions governed by eqn (9) and (10).

$$Al(OH)_3 + OH^- \rightarrow AlO_2^- + 2H_2 \quad (9)$$

$$Al(OH)_3 + 3H^+ \rightarrow Al^{3+} + 3H_2O \quad (10)$$

Consequently, the optimal adsorption pH is determined as 7.0, yielding a calculated capacity of 6.05 mg g^{-1}.

3.6 Solid-to-liquid ratio

Fig. 4e demonstrates an inverse correlation between the solid-to-liquid ratio and adsorption capacity of LiAl-LDHs/ZSM-5: higher ratios correspond to reduced Li^+ uptake. This phenomenon arises from constant Li^+ concentration in solution, consistent with heterogeneous adsorption mechanisms observed in coprecipitation- and hydrothermally-synthesized adsorbents. Consequently, the optimal adsorbent concentration is determined as 10 g L^{-1}, yielding a calculated adsorption capacity of 4.71 mg g^{-1}.

3.7 Comparison of adsorption performance

As demonstrated in Fig. 4f, comparative adsorption experiments under optimized conditions reveal enhanced Li^+ uptake capacity in LiAl-LDHs/ZSM-5 *versus* pristine LiAl-LDHs. This performance elevation confirms that composite formation not only preserves but significantly amplifies adsorption functionality, successfully achieving the modification objectives. The results establish LiAl-LDHs/ZSM-5 as a promising candidate for industrial lithium extraction applications.

3.8 Cyclic performance

As evidenced in Fig. 5a, the LiAl-LDHs/ZSM-5 composite achieved a high Li^+ desorption efficiency of 60.4% under optimal conditions using water elution, demonstrating favorable regeneration performance. Over five consecutive adsorption–desorption cycles, the composite maintained 91.9% of its initial adsorption capacity (Q_1 = 6.42 mg g^{-1}), with Q_5 declining to 5.90 mg g^{-1}. This marginal efficiency reduction (8.1% loss) is attributed to partial active site degradation during cyclic operations. Strategic approaches—such as periodic regeneration or structural modifications—are recommended to enhance long-term stability for practical deployment. The adsorption–desorption principle of aluminum-based adsorbent was given by eqn (11). It can be seen that the adsorption–desorption of aluminum salt adsorbent is a reversible process, which has the characteristics of physical adsorption and chemical adsorption. The regeneration of aluminum salt adsorbent can be realized by washing.[47] This reflects its economic and environmental advantages, as the utilization of water as a desorbent not only reduces costs but also minimizes ecological impact, thereby facilitating industrial cycle sustainability.

$$LiCl{\cdot}2Al(OH)_3{\cdot}nH_2O + H_2O \rightleftharpoons X LiCl + (1 - X)LiCl{\cdot}2Al(OH)_3{\cdot}(n + 1)H_2O \quad (11)$$

3.9 Selective adsorption performance

Lithium extraction from salt lake brines offers the advantages of operational simplicity and low cost. However, the similar

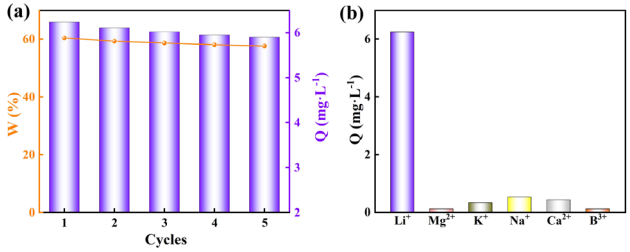

Fig. 5 (a) Cyclic and (b) selective performance of LiAl-LDHs/ZSM-5.

Table 2 Adsorption selectivity of LiAl-LDHs/ZSM-5 for lithium ions

Metal ions	Q_e (mg g^{-1})	K_d (mL g^{-1})	α_{Me}^{Li}	C_F (mL g^{-1})
Li^+	6.24	19.16	1.00	16.08
Mg^{2+}	0.30	0.10	188.13	0.10
K^+	0.11	0.04	478.75	0.04
Na^+	0.22	0.01	1977.78	0.01
Ca^{2+}	0.08	0.24	80.06	0.24
B^{3+}	0.03	0.06	301.33	0.06

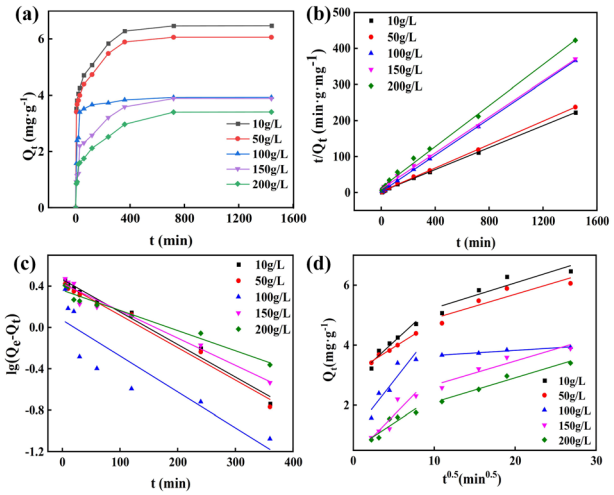

Fig. 6 (a) Curve of adsorption capacity varying with time of LiAl-LDHs/ZSM-5, (b) pseudo-first-order model, (c) pseudo-second-order model, (d) W–M intraparticle diffusion model.

chemical properties of Li^+ and Mg^{2+} pose tough challenges for economically efficient lithium recovery from brines with high Mg^{2+}/Li^+ mass ratios. As shown in Fig. 5b, LiAl-LDHs/ZSM-5 exhibits markedly superior adsorption capacity for Li^+ over competing ions in authentic brine systems, demonstrating exceptional selectivity. The experimentally obtained parameters are presented in Table 2. As can be observed, the distribution coefficient (K_d) of Li^+ is significantly higher than those of other metal ions, indicating the superior selectivity of the adsorbent toward Li^+. Moreover, the competition factor (C_F) of Li^+ was significantly higher than that of competing ions, indicating that GEL-LMO exhibits strong resistance to interference from other ions during lithium-ion adsorption. The selectivity order of LiAl-LDHs/ZSM-5 for each ion follows $Li^+ \gg Mg^{2+} > Na^+ > K^+ > Ca^{2+} > B^{3+}$.This phenomenon can be explained by the adsorption mechanism of LiAl-LDHs: Li^+ ions can enter the solid phase and bind to structural vacancies in LiAl-LDHs, while other impurity ions remain in the liquid phase. LiAl-LDHs is a unique layered material composed of monovalent Li^+ and trivalent Al^{3+} ions. Li^+ ions are embedded in the lattice vacancies within the octahedral framework of $Al(OH)_3$, generating a positively charged structure.[48] Furthermore, due to weak binding affinity on the adsorbent surface, impurities exhibit minimal interference with adsorption efficacy. Consequently, LiAl-LDHs/ZSM-5 demonstrates promising potential for lithium extraction from salt lakes.

3.10 Adsorption kinetics

Kinetic analysis of the adsorption process for the LiAl-LDHs/ZSM-5 composite was performed. The kinetic model curves and corresponding parameters are presented in Fig. 6 and Table 3. As evident from Fig. 6a, the time required to reach adsorption equilibrium increases while the equilibrium adsorption capacity decreases with increasing initial adsorption capacity. The kinetic characteristics are consistent with the conclusions from the previous single-factor experiments. As observed in Fig. 6b and c, the pseudo-second-order model exhibits superior fitting performance compared to the pseudo-first-order model for LiAl-LDHs/ZSM-5, with the calculated adsorption capacity closely matching experimental values. This confirms that the adsorption process follows pseudo-second-order kinetics. Fig. 6d reveals that the W–M curve for Li^+ adsorption does not pass through the origin, indicating a two-stage adsorption mechanism. The initial steep-slope section reflects rapid adsorption dominated by surface diffusion, where abundant active sites lead to high adsorption rates. Subsequently, the plateau section demonstrates slowed adsorption due to site saturation, suggesting intra-particle diffusion contributes to the process but is not the sole rate-limiting step.

3.11 Proposal for the recovery of lithium from salt lake brine

Based on the aforementioned research, this study designed a lithium extraction process (as shown in Fig. 7) from salt lake brine using LiAl-LDHs/ZSM-5. Raw brine collected from salt lakes first undergoes pretreatment to remove impurity ions such as Mg^{2+} and Ca^{2+}, with the solution pH adjusted to 7.0 to optimize adsorption conditions. The conditioned brine then

Table 3 Kinetic parameters of LiAl-LDHs/ZSM-5

Sample	Pseudo-first-order			Pseudo-second-order			Intraparticle diffusion	
C (g L^{-1})	$K_1 \times 10^3$ (min^{-1})	Q_e (mg g^{-1})	R_1^2	$K_2 \times 10^3$ (g mg^{-1} min^{-1})	Q_e (mg g^{-1})	R_2^2	K_3 (mg g^{-1} min$^{-0.5}$)	R_3^2
10	3.15	1.59	0.9821	8.97	6.5	0.9995	0.25/0.08	0.9109/0.7435
50	3.10	1.54	0.9811	9.68	6.13	0.9995	0.17/0.08	0.9830/0.7303
100	3.40	1.00	0.7688	2.90	3.95	0.99995	0.34/0.02	0.8012/0.9503
150	2.60	1.53	0.9603	6.54	3.99	0.9985	0.28/0.08	0.7855/0.8496
200	1.90	1.43	0.9619	6.03	3.51	0.9963	0.18/0.08	0.7772/0.9555

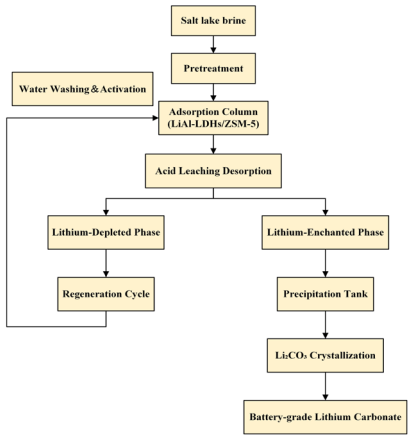

Fig. 7 Technological process of Li^+ extraction from salt lakes by LiAl-LDHs/ZSM-5.

enters an adsorption column where granular LiAl-LDHs/ZSM-5 adsorbent dynamically enriches lithium ions at 25 °C with a solid-to-liquid ratio of 10 g L^{-1}. The lithium-saturated adsorbent is regenerated *via* water elution to obtain a lithium-enriched solution, while the depleted adsorbent can be recycled through washing and reactivation. Finally, the lithium-rich solution undergoes sodium carbonate precipitation and crystallization at 90 °C, yielding battery-grade lithium carbonate with purity exceeding 99.5%. This process demonstrates high adsorption capacity, excellent selectivity, and remarkable adsorbent recyclability, showing significant industrial application potential.

4. Conclusions

The adsorption/desorption performance and selectivity of adsorbents are critical metrics for evaluating their practical applicability. In this work, a ZSM-5 molecular sieve carrier was initially synthesized *via* a seed-assisted method, followed by hydrothermal loading of an aluminum salt adsorbent (LiAl-LDHs) onto its surface, ultimately yielding a composite adsorbent with superior adsorption capabilities. Physicochemical characterization confirmed successful composite formation with an optimal adsorption structure. Adsorption studies revealed optimal conditions for LiAl-LDHs/ZSM-5 as $t = 12$ h, $T = 25$ °C, pH = 7, and $C = 10$ g L^{-1}, achieving an adsorption capacity of 6.24 mg g^{-1}. Desorption experiments showed that the desorption rate was close to 60% kinetic analysis indicated conformity to the pseudo-second-order model ($R^2 > 0.99$), confirming chemisorption as the dominant mechanism. Weber–Morris model analysis revealed that the Li^+ adsorption curve did not pass through the origin, suggesting boundary layer control contributes partially to the process while intra-particle diffusion is not the sole rate-limiting step. This work synergistically combines the structural advantages of molecular sieves with the adsorption properties of layered double hydroxides, providing novel insights for developing high-efficiency adsorbents and offering valuable references for industrial lithium recovery applications.

Conflicts of interest

There are no conflicts to declare.

Data availability

Data are available from the authors upon request.

Acknowledgements

This work was supported by NSFC (No. 22173039), the Liaoning Revitalization Talents Program (XLYC2202040), the Key Technologies R & D Program of Liaoning Provincial Department of Education (LJKZZ20220018), Foundation of Liaoning Provincial Education Department (JYTMS20230760, LJKMZ20220445), the Fundemental Research Funds for Public Universities in Liaoning (LJ242410140002). Doctoral Research Start-up Fund Project of Zaozhuang University (No. 1020733).

Notes and references

1 W. Shi, X. Liu, C. Ye, X. Cao, C. Gao and J. Shen, *Sep. Purif. Technol.*, 2019, **210**, 6.
2 B. Swain, *Sep. Purif. Technol.*, 2017, **172**, 388–403.
3 L. Wang, B. Ji, Y. Hu, R. Liu and W. Sun, *Chemosphere*, 2017, **184**, 594–600.
4 J. Speirs, M. Contestabile, Y. Houari and R. Gross, *Renew. Sustain. Energy Rev.*, 2014, **35**, 183–193.
5 L. Kavanagh, J. Keohane, G. Garcia Cabellos, A. Lloyd and J. Cleary, *Resources*, 2018, **7**, 57.
6 J. Hu, J. Zhang, H. Li, Y. Chen and C. Wang, *J. Power Sources*, 2017, **351**, 192–199.
7 S. E. Kesler, P. W. Gruber, P. A. Medina, G. A. Keoleian, M. P. Everson and T. J. Wallington, *Ore Geol. Rev.*, 2012, **48**, 55–69.
8 C. P. Lawagon, G. M. Nisola, J. Mun, A. Tron, R. E. C. Torrejos, J. G. Seo, H. Kim and W.-J. Chung, *J. Ind. Eng. Chem.*, 2016, **35**, 347–356.
9 H. Vikström, S. Davidsson Kurland and M. Höök, *Appl. Energy*, 2013, **110**, 252–266.
10 S.-Y. Sun, L.-J. Cai, X.-Y. Nie, X. Song and J.-G. Yu, *J. Water Process Eng.*, 2015, **7**, 210–217.
11 Z.-Y. Guo, Z.-Y. Ji, Q.-B. Chen, J. Liu, Y.-Y. Zhao, F. Li, Z.-Y. Liu and J.-S. Yuan, *J. Clean. Prod.*, 2018, **193**, 338–350.
12 T. Hoshino, *Fusion Eng. Des.*, 2013, **88**, 2956–2959.
13 N. Parsa, A. Moheb, A. Mehrabani-Zeinabad and M. A. Masigol, *Chem. Eng. Res. Des.*, 2015, **98**, 81–88.
14 X.-Y. Nie, S.-Y. Sun, Z. Sun, X. Song and J.-G. Yu, *Desalination*, 2017, **403**, 128–135.
15 A. Somrani, A. H. Hamzaoui and M. Pontie, *Desalination*, 2013, **317**, 184–192.
16 N. Heidari and P. Momeni, *Environ. Earth Sci.*, 2017, **76**, 551.
17 Z. Zhou, S. Liang, W. Qin and W. Fei, *Ind. Eng. Chem. Res.*, 2013, **52**, 7912–7917.
18 Z. Zhou, W. Qin, Y. Chu and W. Fei, *Chem. Eng. Sci.*, 2013, **101**, 577–585.

19 Z. Zhou, W. Qin and W. Fei, *J. Chem. Eng. Data*, 2011, **56**, 3518–3522.
20 L. Ji, L. Li, D. Shi, J. Li, Z. Liu, D. Xu and X. Song, *Hydrometall.*, 2016, **164**, 304–312.
21 J. L. Li, H. F. Zhu, M. Wang, L. J. Shi, Y. J. Zhao, H. T. Zhang, F. Ge, W. Q. Kang and J. Gao, *Chin. J. Inorg. Chem.*, 2014, **30**, 2389–2393.
22 Z. Zhou, W. Qin, S. Liang, Y. Tan and W. Fei, *Ind. Eng. Chem. Res.*, 2012, **51**, 12926–12932.
23 B. Swain, *J. Chem. Technol. Biotechnol.*, 2016, **91**, 2549–2562.
24 W. Xiang, S. Liang, Z. Zhou, W. Qin and W. Fei, *Hydrometall.*, 2017, **171**, 27–32.
25 W. Xiang, S. Liang, Z. Zhou, W. Qin and W. Fei, *Hydrometall.*, 2016, **166**, 9–15.
26 R. Chitrakar, H. Kanoh, Y. Miyai and K. Ooi, *Ind. Eng. Chem. Res.*, 2001, **40**, 2054–2058.
27 T. Ryu, J.-K. Shin, J. Ryu, I.-S. Park, H.-J. Hong, B.-G. Kim and K. S. Chung, *Mater. Trans.*, 2013, **54**, 1029–1033.
28 R. Chitrakar, Y. Makita, K. Ooi and A. Sonoda, *Ind. Eng. Chem. Res.*, 2014, **53**, 3682–3688.
29 R. Chitrakar, Y. Makita, K. Ooi and A. Sonoda, *Bull. Chem. Soc. Jpn.*, 2013, **86**, 850–855.
30 S.-Y. Sun, X. Song, Q.-H. Zhang, J. Wang and J.-G. Yu, *Adsorption*, 2011, **17**, 881–887.
31 T. Ryu, D.-H. Lee, J. C. Ryu, J. Shin, K.-S. Chung and Y. H. Kim, *Hydrometall.*, 2015, **151**, 78–83.
32 T. Ryu, J.-C. Ryu, J.-K. Shin, D.-H. Lee, Y. H. Kim and K. S. Chung, *Ind. Eng. Chem. Res.*, 2013, **52**, 13738–13742.
33 S. Wang, X. Chen, Y. Zhang, Y. Zhang and S. Zheng, *Particuology*, 2018, **41**, 40–47.
34 S. Chen, Z. Chen, Z. Wei, J. Hu, Y. Guo and T. Deng, *Chem. Eng. J.*, 2021, **410**, 128320.
35 M. Moazeni, H. Hajipour, M. Askari and M. Nusheh, *Mater. Res. Bull.*, 2015, **61**, 70–75.
36 V. P. Isupov, N. P. Kotsupalo, A. P. Nemudry and L. T. Menzeres, *Stud. Surf. Sci. Catal.*, 1999, **120**, 621–652.
37 X. Liu, M. Zhong, X. Chen and Z. Zhao, *Hydrometall.*, 2018, **176**, 73–77.
38 J. Chen, S. Lin and J. Yu, *J. Hazard. Mater.*, 2020, **388**, 122101.
39 L. Zhang, T. Zhang, Y. Zhao, G. Dong, S. Lv, S. Ma, S. Song and M. Quintana, *Nano Res.*, 2024, **17**, 1646–1654.
40 A. Yamaguchi, D. Jin, T. Ikeda, K. Sato, N. Hiyoshi, T. Hanaoka, F. Mizukami and M. Shirai, *Catal. Lett.*, 2014, **144**, 44–49.
41 H. Hu, Q. Zhang, J. Cen and X. Li, *Catal. Lett.*, 2015, **145**, 715–722.
42 X. Zuo, C. Qian, S. Ma, J. Xiong, J. He and Z. Chen, *Water Sci. Technol.*, 2019, **80**, 507–516.
43 B. Silva, H. Figueiredo, O. S. G. P. Soares, M. F. R. Pereira, J. L. Figueiredo, A. E. Lewandowska, M. A. Bañares, I. C. Neves and T. Tavares, *Appl. Catal., B*, 2012, **117–118**, 406–413.
44 S. Hu, Y. Sun, M. Pu, R. Yun and X. Xiang, *Sep. Purif. Technol.*, 2019, **229**, 115813.
45 J. Milikić, S. Stojanović, K. Rondović, L. Damjanović-Vasilić, V. Rac and B. Šljukić, *Processes*, 2024, **12**, 907.
46 J. Zhong, S. Lin and J. Yu, *J. Colloid Interface Sci.*, 2020, **572**, 107–113.
47 J. Zhong, S. Lin and J. Yu, *Desalination*, 2021, **505**, 114983.
48 T. Graham, J. Hu, X. Zhang, M. Dembowski, N. Jaegers, C. Wan, M. Bowden, A. Lipton, A. Felmy, S. Clark, K. Rosso and C. Pearce, *Inorg. Chem.*, 2019, **58**, 12385–12394.